New Phytologist

Research

Methods

Phenotyping nematode feeding sites: three-dimensional reconstruction and volumetric measurements of giant cells induced by root-knot nematodes in Arabidopsis

Javier Cabrera[1], Fernando E. Díaz-Manzano[1], Marta Barcala[1], Ignacio Arganda-Carreras[2], Janice de Almeida-Engler[3], Gilbert Engler[3], Carmen Fenoll[1] and Carolina Escobar[1]

[1]Facultad de Ciencias Ambientales y Bioquímica, Universidad de Castilla-La Mancha, Av. Carlos III s/n, E-45071 Toledo, Spain; [2]AgroParisTech, UMR1318, Institut Jean-Pierre Bourgin, 78026 Versailles, France; [3]Institut National de la Recherche Agronomique, UMR 1355 ISA/Centre National de la Recherche Scientifique, UMR 7254 ISA/Université de Nice-Sophia Antipolis, UMR ISA, 400 Route des Chappes, 06903 Sophia-Antipolis, France

Author for correspondence:
Carolina Escobar
Tel: +34 925268800 ext. 5476
Email: carolina.escobar@uclm.es

Received: *21 July 2014*
Accepted: *19 November 2014*

New Phytologist (2015)
doi: 10.1111/nph.13249

Key words: Arabidopsis, giant cells (GCs), phenotyping, root-knot nematodes (RKN), three-dimensional reconstruction.

Summary

- The control of plant parasitic nematodes is an increasing problem. A key process during the infection is the induction of specialized nourishing cells, called giant cells (GCs), in roots. Understanding the function of genes required for GC development is crucial to identify targets for new control strategies. We propose a standardized method for GC phenotyping in different plant genotypes, like those with modified genes essential for GC development.
- The method combines images obtained by bright-field microscopy from the complete serial sectioning of galls with TrakEM2, specialized three-dimensional (3D) reconstruction software for biological structures.
- The volumes and shapes from 162 3D models of individual GCs induced by *Meloidogyne javanica* in Arabidopsis were analyzed for the first time along their life cycle. A high correlation between the combined volume of all GCs within a gall and the total area occupied by all the GCs in the section/s where they show maximum expansion, and a proof of concept from two Arabidopsis transgenic lines (J0121 ≫ DTA and J0121 ≫ GFP) demonstrate the reliability of the method.
- We phenotyped GCs and developed a reliable simplified method based on a two-dimensional (2D) parameter for comparison of GCs from different Arabidopsis genotypes, which is also applicable to galls from different plant species and in different growing conditions, as thickness/transparency is not a restriction.

Introduction

The agricultural impact of plant parasitic root-knot nematodes (RKN), particularly of *Meloidogyne* spp., is increasing with the progressive banning of many effective chemicals used for their control. RKN are widespread around the world and can infect thousands of plant species. As the durability of natural resistance genes is in question (Abad *et al.*, 2003), there is an urgent need to search for alternative strategies for their control, such as those based on biotechnology (Fuller *et al.*, 2008; Lilley *et al.*, 2011; Atkinson *et al.*, 2012). Hence, assessing the function of genes putatively involved in crucial processes for the plant–nematode interaction is essential. One of these processes is the formation of specialized nourishing cells, named giant cells (GCs; Jones & Goto, 2011), within the vasculature of the host roots which become hyperplasic and swell, forming a gall or root-knot that encloses them. In order to precisely determine the role of specific genes during GC differentiation and/or maintenance, it is crucial to phenotype these feeding cells and to compare those formed in wild-type plants with those formed in plants with modified gene functions.

GC phenotyping has been based on observations of histological sections from nematode-induced galls embedded in resins, mostly Araldite® (Sigma-Aldrich) or Technovit® (Heraeus Kulzer GmbH, Wehrheim, Germany), using bright-field optics and images collected with digital cameras (de Almeida Engler *et al.*, 2012; Kyndt *et al.*, 2013). To date, data regarding three-dimensional (3D) shape, volume, and changes in these parameters during nematode infection are scarce. This is mainly because of the complex structure in which GCs are embedded within the galls that are surrounded by other tissues, and it is also due to the presence of expanding sedentary nematodes within the galls,

which limits accessibility of the GCs for optical imaging. Another complex, inaccessible structure is the shoot apical meristem (SAM), for which clear 3D reconstructions have been obtained by confocal laser scanning microscopy with different methods (Kayes & Clark, 1998; Grandjean *et al.*, 2004; Chakraborty *et al.*, 2013), but for which cell volume data have only been calculated using serial histological sections (Vanhaeren *et al.*, 2010). By contrast, high-quality volumetric data have been obtained by confocal laser scanning microscopy for other plant structures, for example the root tip meristem (Vanhaeren *et al.*, 2010). Similar to the SAM, GCs present difficulties in terms of accessibility as they are situated in the center of the gall, where the root cortical cells appear to be hypertrophied and the vascular tissues that surround the GCs present abundant tiny asymmetrically dividing cells resulting from continuous cell division as the infection progresses (Bird, 1961; Bleve-Zacheo & Melillo, 1997). Quantitative data on GC shape and size are limited and rely on methods based on two-dimensional (2D) parameters. Thus, no volumetric data are yet available. The physiological status of GCs is closely related to their morphological features, for instance the presence of cell wall ingrowths and wall thickenings. However, currently no standardized methods have been adapted to accurately phenotype GCs. The methods that have been used are based on the measurement of GC diameters over 2D sections (Gal *et al.*, 2006; Das *et al.*, 2008; de Almeida Engler *et al.*, 2012), the areas of individual GCs (Banora *et al.*, 2011; Vieira *et al.*, 2012, 2013; Antonino de Souza *et al.*, 2013; Iberkleid *et al.*, 2013) or the GC pool area as a whole (Vovlas *et al.*, 2005; Wasson *et al.*, 2009; Portillo *et al.*, 2013; Cabrera *et al.*, 2014b), deduced from semi-thin sections. Using these methodologies, differences in GC shape and size were found between wild type and loss-of-function or overexpressing lines. However, these methods are based exclusively on 2D imaging techniques (Kyndt *et al.*, 2013), which have limitations in accurately determining the final GC shapes and volumes.

Three-dimensional representations of the surface of GCs have been obtained based on scanning electron microscopy (Jones & Dropkin, 1976; Orion & Wergin, 1982), which does not allow volume measurements, as only images of the surface are recorded. Three-dimensional representations can be produced from optical sectioning of live or fixed tissue samples by confocal laser scanning microscopy. However, the image quality rapidly decreases when analyzing very thick specimens. In order to improve confocal imaging of GCs, clarifying methods have been applied to enhance undisturbed light penetration, thereby permitting visualization and 3D reconstruction of entire galls, GCs and their nuclei, based on propidium iodide staining (Vieira *et al.*, 2012). However, accurate 3D reconstructions of galls were only obtained down to a depth of 200 μm using Arabidopsis as a host (Vieira *et al.*, 2012). Larger galls, which are typical of late developmental stages, as well as galls induced in different host plants did not allow efficient confocal imaging even after extensive clearing, as a consequence of excessive light absorption and scattering. Two-photon excitation microscopy can generate images deeper inside complex specimens than standard confocal microscopy as a result of long wavelength excitation and more efficient emission light detection. However, this equipment is still not available to many researchers. Moreover, the cell walls of epidermal and cortical cell layers in mature galls are exceptionally light absorbing, greatly limiting the performance of a two-photon microscope. A more recently developed type of microscopy called selective plane illumination microscopy (SPIM) enables the generation of 3D representations of large but relatively transparent biological samples. Use of SPIM allows a significant improvement in live tissue preservation during extensive time-lapse imaging, although there are still limitations in visualizing large specimens such as mature galls. Therefore, the limits set by the 'transport mean free path' of a photon in the gall tissues, as a consequence of absorption and scattering of light, prevent deep 3D imaging with confocal, two-photon or SPIM microscopy.

In this work, we describe a novel approach based on standard microscopy to obtain 3D reconstructions of GCs induced by *Meloidogyne javanica* in Arabidopsis roots at early to late development stages (3, 5, 7, 9, 11, 21 and 40 d post infection (dpi)). The method combines images obtained by conventional light microscopy from the complete serial sectioning of galls with software specialized in the 3D reconstruction of biological structures, TrakEM2 (Cardona *et al.*, 2012). We provide for the first time complete 3D models for all individual GCs within galls and additional important morphological features related to their volume and shape. These results established a reference for the development of a simplified method for GC size comparison, based on 2D images taken from gall sections. This was possible because we detected a high correlation between the combined volume of all GCs within a gall and the total area occupied by all the GCs in the section(s) where they showed their maximum expansion. We demonstrate that this standardized method can be used for comparison of GCs from different Arabidopsis lines and propose that it can also be applied to galls from different plant species and in different growing conditions.

Materials and Methods

Nematode populations

Meloidogyne javanica Treub, 1885 (Portillo *et al.*, 2009) was maintained *in vitro* on cucumber (*Cucumis sativus* L.) plants grown at 28°C in the dark in 0.3% Gamborg medium (Gamborg *et al.*, 1968) supplemented with 3% sucrose. Egg hatching was stimulated in sterile water for 3–4 d.

Plant material, growth conditions and nematode inoculation

Arabidopsis thaliana (L.) Heynh Columbia-0 (Col-0) plants were used throughout this study. Seeds were surface-sterilized with 30% commercial bleach, washed, and sown in 0.3% Gamborg medium (Gamborg *et al.*, 1968) supplemented with 1.5% sucrose. For stratification, plates were kept at 4°C for 2 d and thereafter the plates were kept vertically in a growth chamber at 25°C, 60% relative humidity and in a long-day photoperiod. The plates were inoculated 5 d later just behind each root tip with 7–10 *M. javanica* juveniles per main root. All plants showed only

a primary root when inoculated, therefore having a high growth homogeneity to avoid individual differences. Plants were carefully examined every 12 h under a Leica Mz125 stereomicroscope to establish a penetration and infection timeline, resulting in a maximum error of 12 h when assessing gall age (Barcala *et al.*, 2010). Galls were hand-dissected at 3, 5, 7, 9, 11, 21 and 40 dpi only from the primary root for maximum homogeneity.

Gall fixation and embedding

Galls were rinsed twice for 10 min in sodium phosphate buffer (10 mM; pH 7) and fixed overnight in 3% glutaraldehyde. Dehydration of the galls was carried out in three steps of 15 min in increasing concentrations of ethanol (30, 50 and 70%), two steps of 1 h in 90% ethanol, three steps of 1 h in 100% ethanol and, finally, two steps of 15 min in 100% acetone. Subsequently, galls were embedded in Araldite (Sigma-Aldrich) following several steps of incubation in an Araldite : acetone solution: 2 h in a 1 : 3 solution, overnight incubation in a 1 : 1 solution and three steps of 1 h in a 3 : 1 solution. Finally, the galls were oriented longitudinally in silicone molds filled with 100% Araldite and maintained at 60°C for 48 h for the polymerization of the Araldite. All steps were performed at 4°C.

Table 1 The average number of giant cells (GCs) scored in each developmental stage, and the average number of sections obtained for a complete sectioning of every GC within a gall induced by *Meloidogyne javanica* in *Arabidopsis thaliana* roots

Days post infection (dpi)	No. of GCs	Average no. of sections
3	20	20
5	19	25
7	19	51
9	33	43
11	26	59
21	23	74
40	22	99

Gall sectioning and image capture

Galls at 3, 5, 7, 9, 11, 21 and 40 dpi were fully sectioned at 2 µm with a diamond knife in an ultramicrotome (Microm HM360; Thermo Scientific, Waltham, MA, USA). Correlative longitudinal sections were carefully recovered and placed one by one on glass slides. Sections were stained for 5 min with 1% toluidine blue in 1% borax solution (TAAB) at 40°C. High-quality micrographs (0.2 µm pixel^{-1}) of the 2-µm sections containing GCs were obtained at ×10 magnification under a light microscope (Nikon Eclipse 90i) equipped with a digital camera (Nikon Dxm 1200c). TrakEM2 software provided together with the Fiji image processing toolbox was downloaded from http://fiji.sc/Fiji and used for sample alignment and 3D gall reconstruction. Most of the pre-established parameters of the software were maintained for all the samples reconstructed, with the exception of: pixel width (0.2 µm), pixel height (0.2 µm) (thus, resolution is 0.2 µm pixel^{-1} on the *x*/*y*-axis), voxel depth (2 µm), steps per scale (5), feature descriptor size (8), maximum alignment error (50) and iterations for mesh smoothing (15). Measurements of volume, area, maximum diameter or surface area of the GCs were calculated by TrakEM2 depending on the number of pixels occupied by each GC.

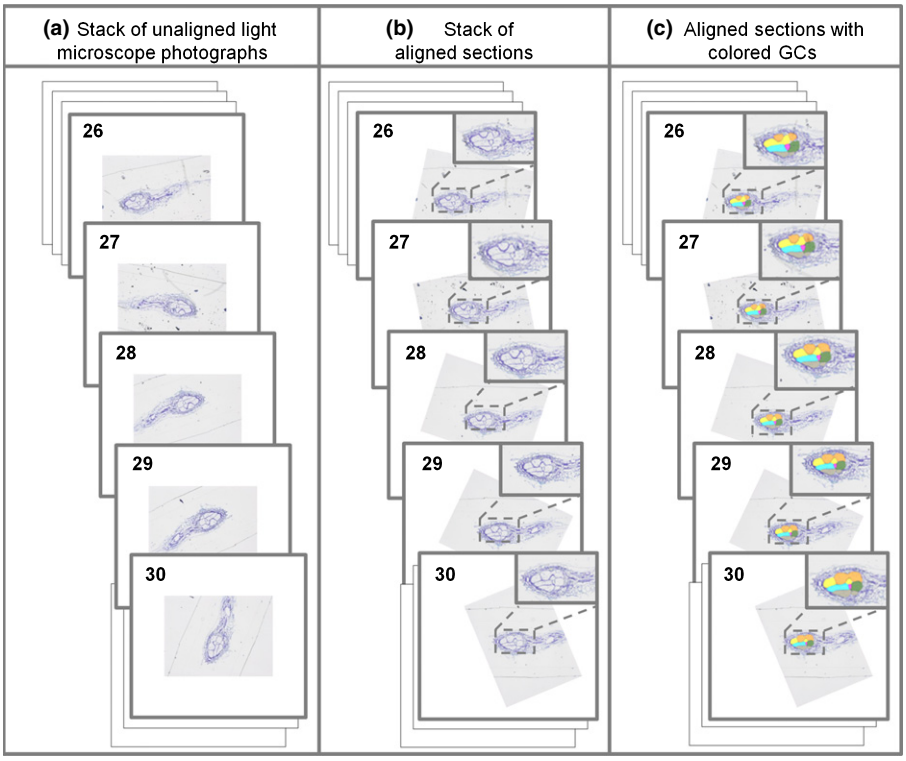

Fig. 1 Three basic steps of section processing prior to the three-dimensional (3D) reconstruction of a gall induced by *Meloidogyne javanica* in Arabidopsis. Five representative sections of the whole 2-µm section series (indicated by numbers) from a gall stained with toluidine are shown. (a) Consecutive nonaligned images. (b) Consecutive aligned images. (c) Consecutive aligned images with giant cells (GCs) labeled. The color code for each GC was maintained in all the consecutive sections as indicated. See Supporting Information Video S1 for a detailed view of the process.

New Phytologist

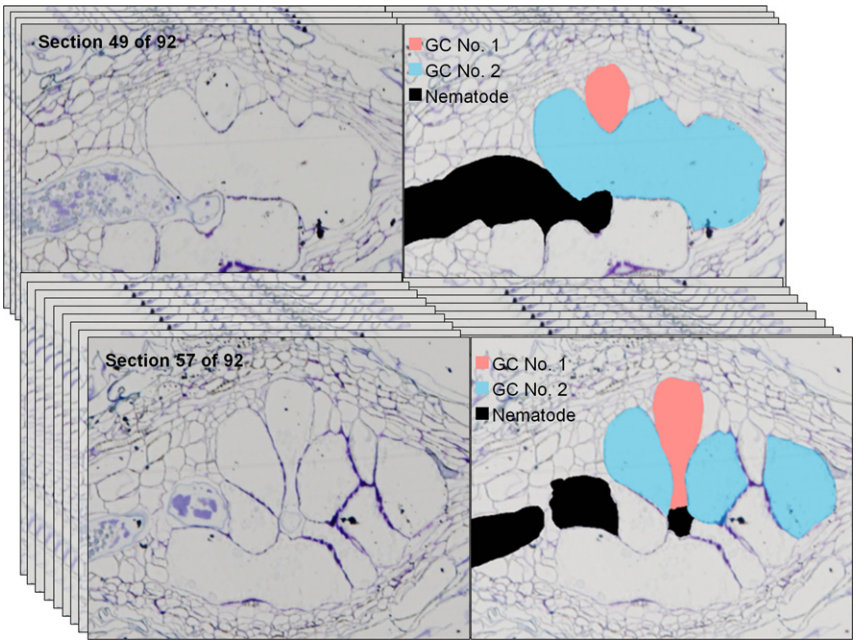

Fig. 2 Serial sectioning of an Arabidopsis gall induced by *Meloidogyne javanica* with aligned images and colored giant cells (GCs) (numbers indicated at the top left of the images). Two-micrometer sections are stained with toluidine. This method enables detailed characterization of cell morphology across the series (left panels, only toluidine staining; right panels, colored cells). It avoids misinterpretation arising from the observation of single isolated sections or a small group of sections. The blue cell in section 49 could be misinterpreted in section 57 as three independent GCs. The pink cell that in section 49 is distant from the nematode appears to be in direct contact in section 57. See Supporting Information Video S2 for a detailed view.

Table 2 Volume data for the giant cells (GCs) induced by *Meloidogyne javanica* in *Arabidopsis thaliana* roots analyzed in each developmental stage

	Giant cell volume ($\mu m^3 \times 1000$)						
Giant cells scored	3 dpi	5 dpi	7 dpi	9 dpi	11 dpi	21 dpi	40 dpi
1	51.08	429.04	264.24	1706.60	1222.61	1266.25	898.34
2	78.10	103.77	477.94	434.32	777.58	706.38	862.16
3	64.98	208.38	280.76	675.00	372.13	32.39	1578.19
4	34.52	297.64	491.99	414.31	239.64	1002.97	1475.63
5	33.10	181.72	802.90	711.56	1524.61	755.42	653.03
6	44.03	79.24	157.66	450.44	169.88	239.34	5515.04
7	119.83	153.66	422.48	208.10	7.08	461.10	432.55
8	56.92	35.45	705.58	159.68	42.41	4284.63	2470.65
9	44.00	81.19	946.48	759.53	66.31	7178.51	5025.32
10	197.45	47.31	118.08	881.92	690.28	1467.47	4290.73
11	35.04	174.20	223.68	550.18	825.08	2438.88	5380.71
12	23.44	14.27	556.00	1035.09	103.00	1811.96	7484.93
13	19.99	22.52	364.17	119.77	194.19	4417.29	6426.85
14	22.36	13.59	188.85	259.01	113.74	1942.30	14 537.59
15	16.87	17.44	392.07	427.42	261.62	822.25	980.73
16	63.01	15.25	186.02	547.25	142.68	679.39	1273.03
17	48.43	16.57	238.31	197.75	169.92	534.44	1886.69
18	46.60	11.90	564.68	100.13	907.22	985.97	984.86
19	83.69	29.14	301.89	163.82	1609.97	2646.93	1354.74
20	12.19			133.19	2887.99	543.58	1177.22
21				69.74	2213.99	523.17	3200.48
22				91.36	1138.09	2600.88	464.22
23				396.02	3875.18	1362.92	
24				196.98	1924.14		
25				126.28	1847.33		
26				633.60	1252.40		
27				210.35			
28				238.47			
29				73.83			
30				83.45			
31				325.51			
32				154.63			
33				590.57			
Average volumes	54.78	101.70	404.41	397.75	945.35	1682.80	3106.99

dpi, days post infection.

Results and Discussion

GC labeling from gall serial sections using TrakEM2

Herein, we used a simple technique to obtain a 3D overview of RKN-induced GCs, analyzing their phenotypic characteristics and the volume that they occupy during nematode life cycle progression. A total of 2240 longitudinal histological sections (2 μm thick) from 162 GCs in seven different stages of gall development (3, 5, 7, 9, 11, 21 and 40 dpi) (Table 1) were processed. The average number of sections obtained from the complete sectioning of every GC within a gall increased during development (from 20 at 3 dpi to 99 at 40 dpi; Table 1). The stack of light microscope photographs obtained was imported into TrakEM2 (http://fiji.sc/TrakEM2), software that allows 3D modeling from histological serial sections (Fig. 1a; Supporting Information Video S1). TrakEM2 has been successfully used in other research fields, as in the reconstruction of neuronal circuits in *Drosophila* (Cardona *et al.*, 2012). It is publicly available for download together with the Fiji image processing toolbox (an open source image processing package based on ImageJ (US National Institutes of Health, Bethesda, MD, USA), widely used for microscopy image processing; Schindelin *et al.*, 2012; Schneider *et al.*, 2012), in contrast to commercial software previously used in 3D reconstructions in Arabidopsis (Vanhaeren *et al.*, 2010). For optimal GC recognition, all sections were rotated and translated to perfectly align them onto each other by making use of the tools for free affine transforms provided by TrakEM2. The high similarity between consecutive sections allowed TrakEM2 to analyze their pixels for similar features and rigidly transform (rotate and/or translate) the upper image for an optimal match over the consecutive image on the bottom (compare Fig. 1a and b; Video S1). This process was repeated consecutively down through all the sections to the end of the stack. The alignment of consecutive sections made it easier to define each GC within a gall and, by making use of the area list tool, to label it manually with a color code which was used in all the consecutive sections in which that particular GC could be distinguished (Fig. 1c; Video S1). Detailed step-by-step video tutorials on the use of TrakEM2 created by the authors in collaboration with the software developers are available at http://fiji.sc/TrakEM2_tutorials.

This alignment proved to be particularly useful to avoid misinterpretation of GC number and size, as individual GCs could be traced along the entire gall. In this way, multiple GCs can be unambiguously identified, allowing one to distinguish between multiple GCs and those individual cells that in some 2D sections seemed to be more than one as a consequence of the presence of interspersed vascular cells. See, for instance, the blue GC in Fig. 2 which turned out to represent a single cell with protrusions (Fig. 2, blue GC; Video S2). The GC position with respect to the nematode (Fig. 2, pink GC) could also be clearly determined; for example, a GC that in a given section seemed to be far away from the nematode was found to be adjacent to the parasite when seen in some of the subsequent sections in which this cell appeared (Fig. 2, pink GC). Usually, GCs contained a zone with an elongated tube-like structure in the area adjacent to the nematode, in contrast with the more rounded and expanded shapes that they presented in the area more distant from the nematode (Figs 2, 4i–l). This strongly suggests that all GCs have been in contact with the nematode at some stage of the gall development. Thus, we determined the exact number of GCs in each gall, again avoiding misinterpretations arising from those sections where GCs were interspersed with other cells. We found that the number of GCs was not correlated with the stage of development

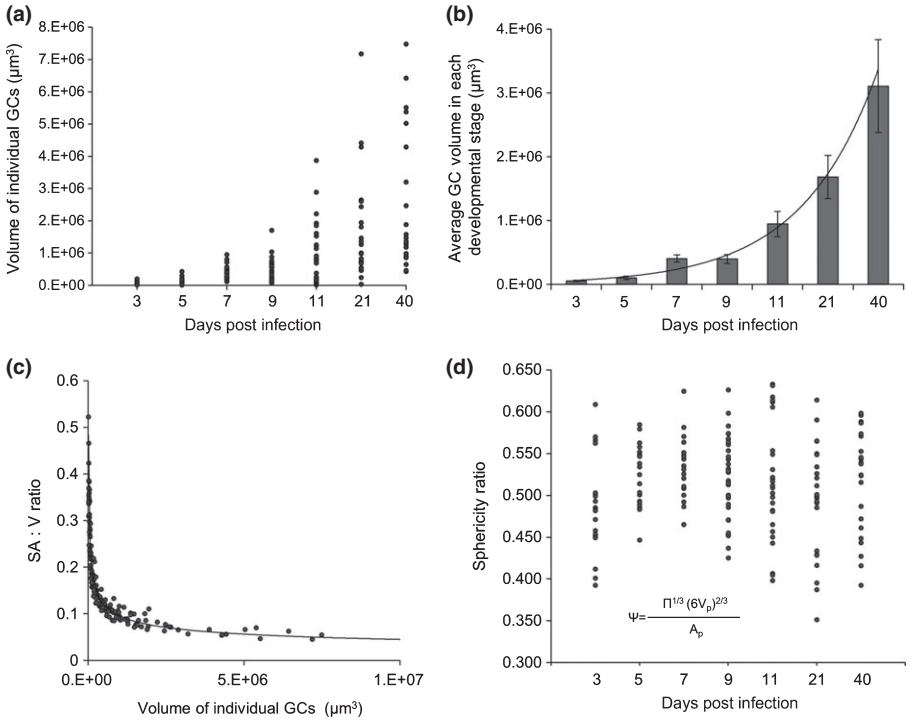

Fig. 3 Volume evolution, sphericity and surface area to volume ratio (SA : V) of giant cells (GCs) formed by *Meloidogyne javanica* in Arabidopsis along infection time. (a) Volume of each of the individual 162 GCs reconstructed. (b) The average volume occupied by all the GCs corresponding to the same developmental stage. (a, b) The *x*-axes in the two graphs indicate galls at different infection stages: at 3 ($n = 20$), 5 ($n = 19$), 7 ($n = 19$), 9 ($n = 33$), 11 ($n = 26$), 21 ($n = 23$) and 40 d post infection (dpi; $n = 22$); in (b) bars indicate ± SE. (c) The ratio of the total surface area (SA) to the final volume (V) occupied by single GCs (SA : V ratio). The ratio becomes smaller as the volume increases. (d) Sphericity (Ψ) measurement of the GCs at the different stages of development. Note that sphericity is different in each GC at all developmental stages indicated. Vp, volume of the GC; Ap, surface area of the GC.

(Table 1). These observations reinforce the idea that, once the nematode is sedentary within the vascular cylinder, differentiation of those selected cells into GCs is in progress and almost no new GCs will be induced at later infection stages. This suggests that the nematode moves its head from one cell to another for nutrient uptake until it has completed its life cycle (Bleve-Zacheo & Melillo, 1997; Grundler & Böckenhoff, 1997).

In summary, using TRAKEM2 we aligned histological sections from galls induced by RKN in Arabidopsis, facilitating the identification and observation of the GCs within the gall and reducing the multiple sources of misinterpretation regarding their number and position. This method also allowed the easy collection of accurate qualitative and quantitative data from histological sections that are essential for GC phenotyping, as shown in the following sections.

Three-dimensional reconstruction and volume estimation of GCs

After aligning and assigning a color code to each GC, 3D models of GCs were generated using the IMAGEJ 3D Viewer (Schmid *et al.*, 2010), integrated in TRAKEM2 (Fig. S1). All the 3D models obtained in this work can be visualized and handled online at https://sketchfab.com/jcabrerachaves/models. In addition to the visualization of the morphological characteristics of the cells, one of the most valuable applications of the 3D reconstruction is the extraction of volumetric data (Table 2). We measured the volumes of 162 GCs obtained from 2240 independent sections at seven different stages (3, 5, 7, 9, 11, 21 and 40 dpi). They ranged from 7081 μm^3 (11 dpi) to 14 537 585 μm^3 (40 dpi; Table 2). Interestingly, the volume of individual GCs did not always correlate well with the stage of gall development (Table 2; Fig. 3a). However, the average volume occupied by all the GCs as a pool within a gall at each infection time showed a clear tendency to increase as the infection progressed, with a positive correlation between the two variables (see exponential line tendency in Fig. 3b). This suggests that individual GCs grow asynchronously during gall development, perhaps as a result of mechanical restrictions or of differential stimulation by the nematode. GC volumes at the early stages of development were more homogenous than the volumes of older GCs (Fig. 3a,b). Individual variability may buffer differences between some developmental stages; for example, there was a large increment in size from 9 to 11 dpi, but the size of the GCs did not vary much from 3 to 5 dpi or from 7 to 9 dpi. All these findings emphasize the importance of the GC pool within a gall, as a whole functional 'pseudo-organ'.

The surface area and the surface area to volume ratio (SA : V) for each GC were obtained after the reconstruction (Fig. 3c). The diffusion rate of solutes is proportional to the surface area, and larger cells of similar shape will have slower diffusion rates than smaller cells. Thus, the higher the cell SA : V ratio, the more effective solute exchange should be, and therefore a higher metabolic activity could be maintained. The SA : V ratio of GCs decreased as size increased, from values above 0.4 in the smallest cells to values under 0.1 in the largest ones (Fig. 3a). Studies of their protein content indicated that the maximum metabolic activity within the GC coincides with the egg-laying stage (Bird, 1961), when the feeding cells are fully expanded. Accordingly, Class I small heat-shock proteins (sHSPs) are highly abundant in developed GCs as compared with the rest of the gall, correlating with the activation of several *sHSP* promoters in the medium–late developmental stages. These chaperones may be related to the maintenance of proper protein folding, preventing the aggregation of abundantly synthesized proteins in highly active cells (Escobar *et al.*, 2003; Barcala *et al.*, 2008). Thus, the coincidence in time of low SA : V ratios and high metabolic activities is apparently a contradiction, but the extensive formation of wall ingrowths at medium–late developmental stages could be a response to a clear functional requirement to compensate for the decrease in the SA : V ratio as the cells expands. Thus, an increase in the effective solute exchange area is achieved through the differentiation of the GCs into transfer cells (Jones & Northcote, 1972; Jones & Gunning, 1976; Cabrera *et al.*, 2014a). Yet, the increase in their plasma membrane surface area may be up to 20-fold (Jones &

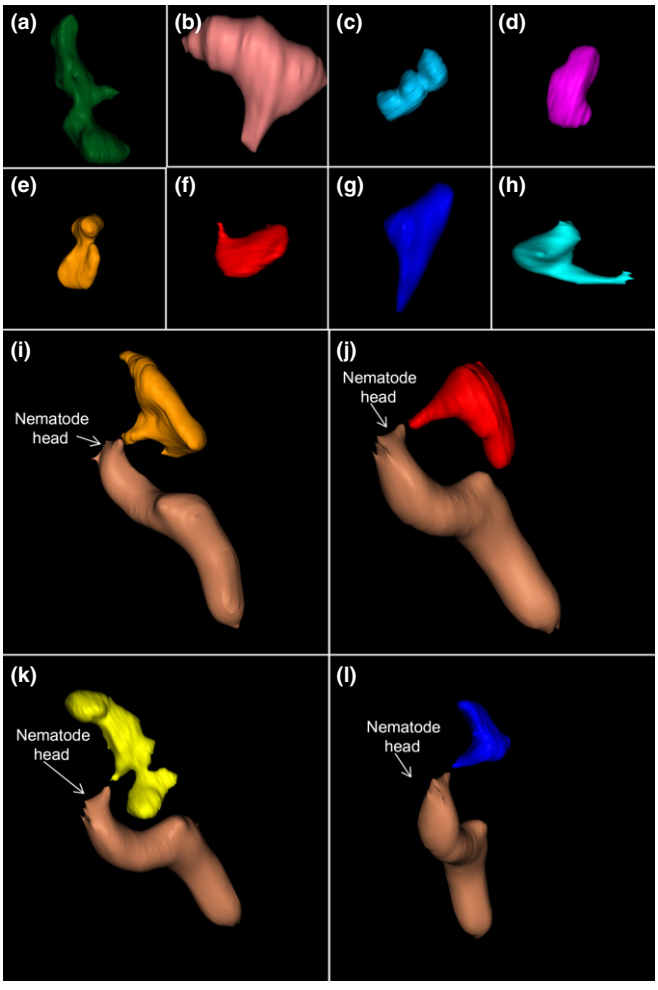

Fig. 4 Representative samples of reconstructed giant cell (GC) shapes. (a–h) Three-dimensional (3D) reconstruction showing the highly diverse morphology of the GCs at (a) 21, (b–f) 7 or (g–h) 5 d post infection (dpi). Note the remarkably irregular shapes in (a–h). (i–l) Three-dimensional reconstruction of GCs together with the nematode. A protruding GC end next to the nematode head is always observed. The shape of the nematode corresponds to the cavity left in each section by the nematode body, as it is normally retracted during the embedding process.

Goto, 2011). In this respect, for the functional characterization of particular genes during gall formation, it might be worth examining the cell wall ingrowths even if the GC size is not altered in loss-of-function lines as compared with controls, as suggested by Cabrera *et al.* (2014a).

To further investigate GC morphology, we also calculated the sphericity of GCs at the different developmental stages studied. Sphericity, a measure of the roundness of an object, is defined as the ratio of the surface area of a sphere (having the same volume as the object of interest) to the surface area of the object; hence the sphericity of a sphere should be 1 (Girshovitz & Shaked, 2012). Our results showed that the shape of GCs, measured in terms of their sphericity, seemed to be the same throughout gall development (Fig. 3d). No spherical cells were found in our study, as values of sphericity ranged between 0.4 and 0.7 for all the GCs characterized (Fig. 3d). In fact, the shape of some GCs was clearly more elongated than spherical (Figs 4, S1). As, for the same volume, spherical cells will have slower diffusion rates than elongated cells (Young, 2006), the shape of GCs could be another way to compensate for the low SA : V ratio of GCs at late developmental stages. The low sphericity values were also consistent with the presence of abundant protuberances and crevices which produced an irregular shape and prevented GCs from becoming spherical, as clearly illustrated in the 2D sections and 3D models (Figs 2, 4a–h, S1). This might be attributable to mechanical constraints imposed by the presence and feeding activity of the nematode and other vascular cells which push and pull the GCs as galls develop. However, some common features were identified among the GCs, such as an elongated protuberance from the main body of the GC adjacent to the nematode head (Fig. 2), which is more easily appreciated in the 3D reconstruction (Fig. 4i–l). These protuberances might be associated with the accumulation of microtubules and organelles close to the nematode head observed during *in vivo* monitoring of galls harboring GFP fusions (de Almeida Engler *et al.*, 2004).

The diameter of GCs within Arabidopsis galls may range from 100 to 500 μm at late developmental stages (40 dpi). They can be even larger in galls within other plant hosts such as cowpea (*Vigna unguiculata* (L.) Walp.) or tomato (*Solanum lycopersicum* L.) (Gal *et al.*, 2006; Das *et al.*, 2008), hampering the generation of high-quality 3D projections of a complete GC for accurate volume quantification using 3D confocal projections of serial optical sections. Thus, 3D reconstructions of GCs with the method presented here proved to be very useful for accurate measurement of GC volumes and identification of their morphological characteristics. This also represents a step forward in the phenotyping of feeding cells, providing valuable and standardized information on the number, shape, position and volume of GCs and minimizing misinterpretations arising from the use of 2D images. The method could easily be applied to galls of different plant species having different thicknesses, providing that the tissues are well fixed to maintain gall morphology in the sections.

Correlation between pooled GC area in single sections and total GC volume within a gall: a simplified standardized phenotyping method

The abovementioned results demonstrate that GC phenotyping provides valuable information in addition to the currently performed infection tests. While methods for studying nematode resistance or susceptibility with infection tests are fairly well understood and established, no standardized methods exist for the detailed phenotyping of GCs. In our study, the volumes of the GCs induced by an RKN within a gall have been accurately measured for the first time; this method provides an effective means of analyzing in depth the phenotypic differences between GCs.

Table 3 Compilation of studies on the interaction between root-knot nematodes and plants

Method	Reference	Species	Days post infection (dpi)	Number of samples
Comparison of the size of the GCs by visual observation from gall sections. No measurements made	de Almeida Engler *et al.* (2004)	Arabidopsis (*Arabidopsis thaliana*)	40	–
	Caillaud *et al.* (2008)		10	
	Clement *et al.* (2009)		7, 21	
	de Almeida Engler *et al.* (2012)		7, 21	
	Pegard *et al.* (2005)	Pepper (*Capsicum annuum* L.)	5	
	Anwar & McKenry (2007)	Cotton (*Gossypium hirsutum* L.)	–	
	Souza Ddos *et al.* (2011)	Tobacco (*Nicotiana tabacum* L.)	8	
Measurement of GC diameter from sections	Gal *et al.* (2006)	Tomato (*Solanum lycopersicum* L.)	42	10 galls
	Das *et al.* (2008)	Cowpea (*Vigna unguiculata* L.)	5, 9, 14, 19, 21	3 GCs
Measurement of the area occupied by individual GCs in gall sections	Banora *et al.* (2011)	Arabidopsis (*Arabidopsis thaliana*)	7, 14, 21	60 GCs
	Vieira *et al.* (2012)		14, 18, 40	25 GCs
	Vieira *et al.* (2013)		7, 14, 21, 40	60 GCs
	Iberkleid *et al.* (2013)	Tomato (*Solanum lycopersicum* L.)	5, 15, 28	50 GCs
	Antonino de Souza *et al.* (2013)	Tobacco (*Nicotiana tabacum* L.)	14	21 GCs
Measurement of the total area occupied by the pool of GCs within gall sections	Vovlas *et al.* (2005)	Chickpea (*Cicer arietinum* L.)	30	24 sections
	Portillo *et al.* (2013)	Tomato (*Solanum lycopersicum* L.)	15	20 sections
	Cabrera *et al.* (2014a)	Arabidopsis (*Arabidopsis thaliana*)	14	20 sections

Differences in the giant cells (GC) size between wild type and loss-of-function or overexpressing lines inferred from two-dimensional sections were investigated with different methods. The methods used to phenotype the GCs are explained in the first column. The plant species, dpi and number of GCs or galls scored are indicated in the other columns.

Recent studies (summarized in Table 3) investigated differences in GC size between wild type and loss-of-function or overexpressing lines by inference from 2D gall sections. Our results presented here demonstrate that there are multiple sources of misinterpretation of data from 2D gall sections, such as those related to the number, position and shape of GCs (Fig. 2). Several of these studies did not provide quantitative measurement of the GCs, but compared their sizes by direct, qualitative observations of 2D sections (Table 3). Other studies collected various quantitative data from gall sections. Three different parameters were used: the maximum diameter of the GCs, the maximum area occupied by individual GCs and the maximum area of all GCs as a pool in selected gall sections (Table 3). The present study has shown that GC morphology is extremely irregular (Figs 4, S1). Thus, inferring differences in GC size from 1D or 2D parameters such as the diameter and area seems not to provide sufficient accuracy. By contrast, the volume data obtained in this study allowed us to determine with high accuracy the size and 3D structure of GCs. However, 3D reconstruction of GCs within a gall is a tedious, demanding and time-consuming task because of the need to process many sections per gall (Table 1; Figs 1, 2; Videos S1, S2). Therefore, a simpler method is still needed.

To this end, we investigated the correlation between GC volumes obtained in this work and other parameters used to phenotype the GCs. The maximum diameter, provided by the software after reconstruction, showed a poor Pearson correlation index of 0.61 ($P < 0.05$) (Fig. 5a), whereas a much higher correlation (0.93; $P < 0.05$) was obtained between the volume and the area of the individual GCs measured in the section where they showed maximum expansion (considering maximum expansion as the section where a specific GC showed its largest area from all the sections in which it was colored; Fig. 5b). The maximum correlation indexes were obtained between the volume of the total pool (considering the sum of all the GCs) contained in a gall and the area of the GC pool in the section

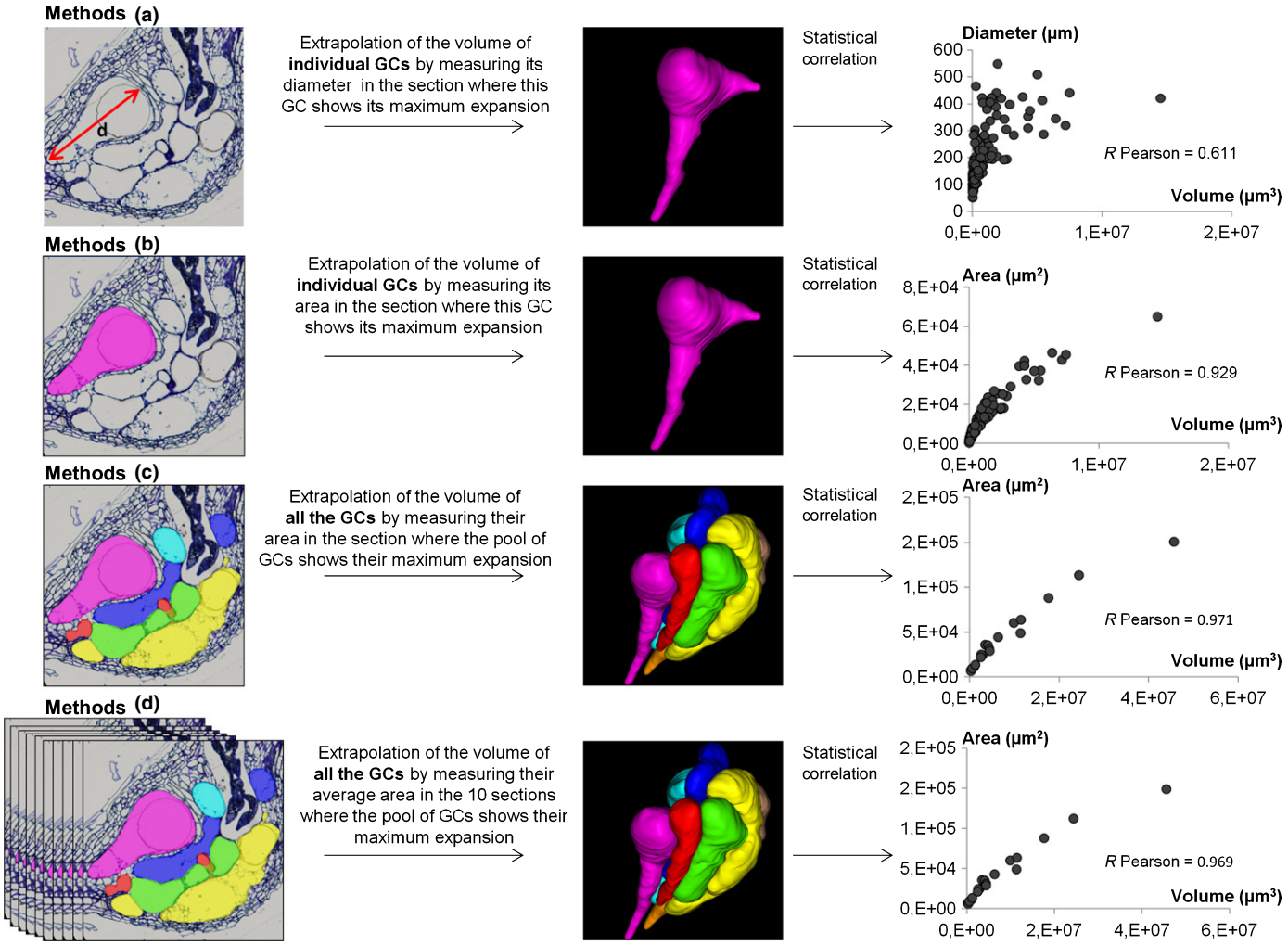

Fig. 5 Giant cell (GC) diameter, area and volume correlations. Correlations are shown between (a) the diameter and the volume of individual GCs, (b) the volume and the area of maximum expansion of individual GCs, (c) the volume of the total GC pool within a gall and the GC pool area in the section showing its maximum expansion, and (d) the volume of the GC pool within a gall and the average GC pool area in the 10 sections where GCs showed their maximum expansion. For all Pearson correlation coefficients shown, $P < 0.05$. Left panels, sections with those cells measured colored; middle panels, three-dimensional reconstructions; right panels, graphs representing the correlations described.

showing maximum expansion (0.97; $P < 0.05$; Fig. 5c). Interestingly, a similarly high correlation value (0.97; $P < 0.05$) was also obtained between the volume of the GC pool contained in a gall and the average area of the pool of GCs from the 10 sections where the pool of GCs showed their maximum expansion (Fig. 5d).

Extrapolation of the volumes from the 2D parameters presented some technical difficulties. For instance, the identification of sections where GCs show their maximum expansion area is difficult if a previous labeling and alignment of the correlative sections obtained from a gall is not performed. In some of the references given in Table 3, only two to three GCs per gall were chosen for area measurement. If individual GCs are selected, the striking differences in volume among GCs of the same age demonstrated here (Fig. 3a; Table 2) are not taken into account. If the whole volume occupied by the GC pool within a gall is not measured, this may introduce significant errors. Nevertheless, the choice of the section with maximum area occupied by the GC pool also would require the measurement of all the sections of a gall to avoid misinterpretations leading to errors.

For all these reasons, we propose a simplified method that minimizes these problems and speeds up the processing considerably. The method is based on a 2D parameter that shows a high correlation with the final volume of the GC pool. We showed that the average area occupied by all the GCs within a gall from the 10 sections with the maximum expanded GC pool had a high correlation with the pooled GC volume (Fig. 5d). By using an algorithm in which the areas of two of these 10 sections with

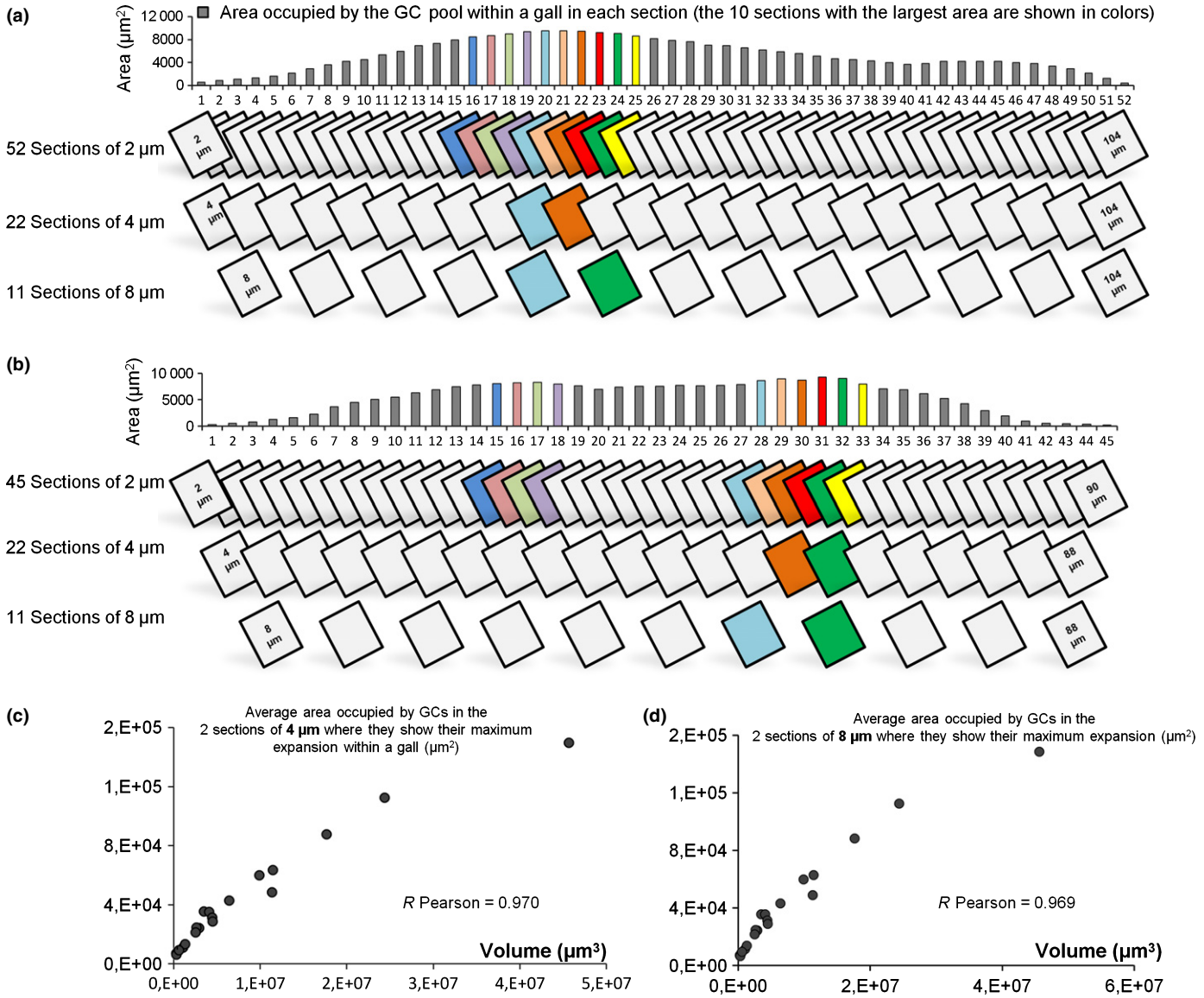

Fig. 6 Schematic representation of the simplified method for giant cell (GC) size phenotyping. Serial sections of the two main types of gall (a, b) detected in this study (one-dome or two-dome shape). The 10 sections with the largest GC expanded area are colored. (c) Correlation between the average GC pool area of the two sections of 4 µm with maximum GC expansion (*y*-axis) and their volume (*x*-axis) was high. (d) The same as (c) but with sections of 8 µm. Pearson correlation coefficients: $P < 0.05$.

maximum expanded GC pool are randomly selected with 1000 iterations (Wichman & Hill, 1982), we obtained high correlations between the two parameters (pooled GC area and volume): a minimum correlation index of 0.968 and a maximum of 0.972. The identification of two random sections among those 10 sections with the largest area occupied by the GC pool within a completely sectioned gall can be performed easily, accurately and with minimum errors. To further facilitate large-scale GC phenotyping, the number of sections obtained from a gall should be minimized, as processing an entire gall into 2-μm-thick sections is tedious work. Using 4–8-μm-thick sections, the number of sections for each gall would dramatically decrease (two to four times less than at 2 μm); for example, from 100 sections to 50 or 25. Moreover, differences in the area occupied by the GC pool among thicker sections are easily determined by simple visual inspection. Fig. 6 shows schematically the reduction in the number of sections obtained from two different types of gall (a and b), which were artificially classified depending on their GC area distribution. In Fig. 6(a), the sections with the maximum GC area are correlative, whereas in (b), there are two groups of sections with maximum areas. Those shapes were selected among the 162 GCs scored, as shown in more detail in Fig. S2. When a gall is processed in 4-μm-thick sections, and sections with the maximum GC area are selected, at least two of the sections will be among those 10 with the maximum GC area from the gall if it were sectioned at 2 μm (shown with a high area : volume correlation; Figs 5d, 6c). Similar results were obtained for 8-μm sections (Fig. 6d) and for 5–7-μm sections (data not shown). Thus, by selecting and measuring the area of the GC pool in the two sections with the highest GC expansion from either 4- or 8-μm-thick sections (easily identified at first glance, as the differences between sections are greater than at 2 μm), the correlation index with the GC volume was maintained at 0.97 ($P < 0.05$) in both cases (Fig. 6c,d). This simplified method that we propose reduces the number of gall sections necessary for large-scale phenotyping while maintaining a very high accuracy. The method is based on a 2D parameter (the area of the GC pool within a gall) that we demonstrated to be proportional to the size measured as the total GC volume developed by *M. javanica* inside the gall. Therefore, this method will be useful for comparison of GC phenotypes in terms of their size among different plant genotypes and/or plant species.

A proof of concept: simplified GC phenotyping method applied to a specific case in Arabidopsis

In order to confirm the utility of the simplified method, we compared the size of GCs from galls induced by *M. javanica* in the transgenic line J0121 ≫ DTA (where GCs are genetically ablated by the expression of the diphtheria toxin A in the GCs)

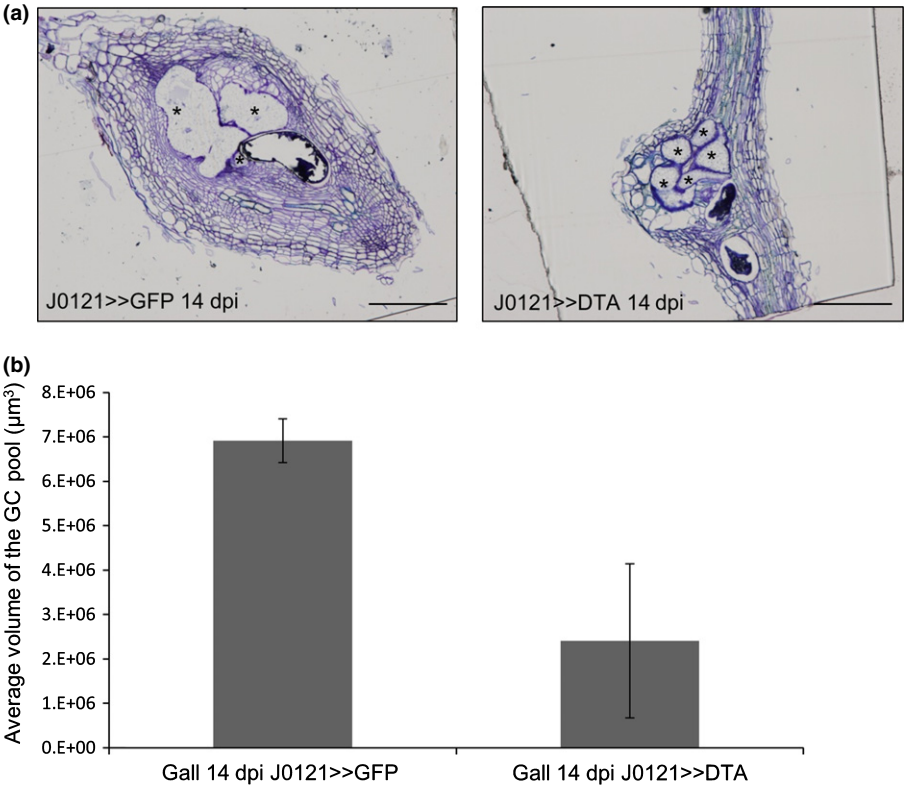

(c)

	Average volume of the GC pool (μm³)	Average area of the 2 largest sections per gall (μm²)
Gall 14 dpi J0121>>DTA	2407069.6	16794.7
Gall 14 dpi J0121>>GFP	6915912.6	31900.5

Fig. 7 A proof of concept: simplified giant cell (GC) phenotyping method applied to a specific case. (a) Toluidine-stained 4-μm representative sections of galls from each Arabidopsis line as indicated: J0121 ≫ GFP and J0121 ≫ DTA. Bars, 50 μm. Asterisks indicate GCs (b) Histograms indicate the average volume occupied by the GC pool from two representative galls of each line as indicated (± SE). (c) The average volume and the average area of the two largest sections per gall for each genotype are also indicated in the small table underneath. dpi, days post inoculation.

with that in the control line J0121 ≫ GFP (expressing GFP within the GCs) [Correction added after online publication 22 January 2015: the preceding sentence has been corrected]. In a previous work, we found that the GC pool in J0121 ≫ DTA was smaller than that in the control line J0121 ≫ GFP, based on the GC pooled area measured in 4-μm-thick single sections (Cabrera *et al.*, 2014b); however, 3D reconstructions were not generated. In the present work, we reconstructed J0121 ≫ DTA GCs from 14-dpi galls and from the control J0121 ≫ GFP (Fig. 7a) using 4-μm sections. The average volume occupied by the GC pool was at least 2-fold larger in the control line than in J0121 ≫ DTA (Fig. 7b). When the GC pool areas from the two sections with the maximum GC expansion (Fig. 7c) among all sections obtained from each gall were compared, the same difference between the two lines (*c.* 2-fold) was obtained as when using their total GC volumes (Fig. 7c). This is expected from the high correlation (Pearson correlation coefficient $R = 0.97$; $P < 0.05$) between the two parameters that we found (see previous section). Thus, we confirmed that a 2D measurement (area of the GC pool from the two sections with the maximum expansion area of the GCs) selected by visual inspection is a valid parameter to use to compare GC sizes between two different plant genotypes. The shapes of the individual GCs from the J0121 ≫ GFP control line and the J0121 ≫ DTA line (Fig. 8a,b) were similar, and no differences in the typically irregular shape were evident.

This example further confirms that the simple, fast and easy standardized method proposed here is very effective for detection of phenotypic differences between GCs from different

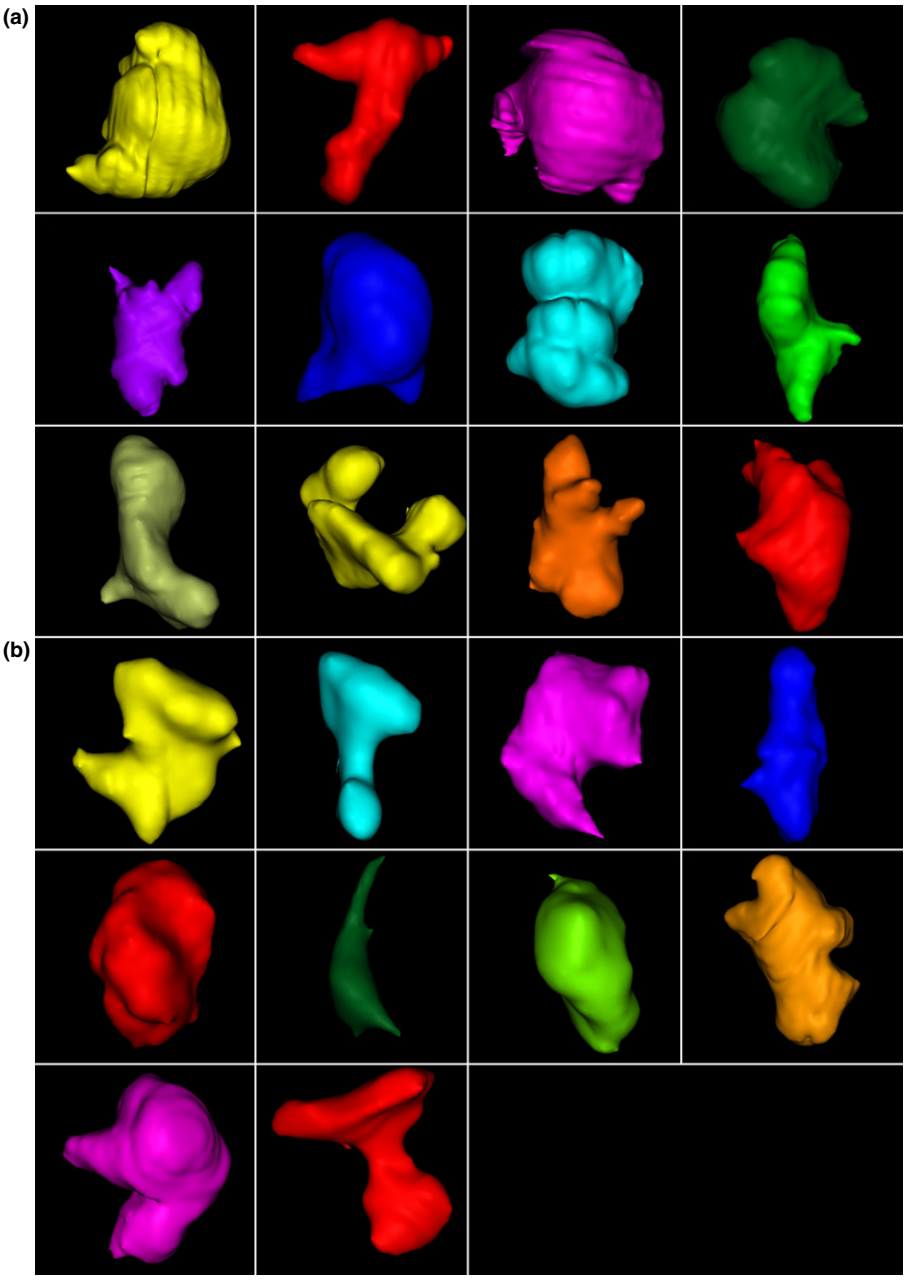

Fig. 8 Three-dimensional reconstruction of individual giant cells (GCs) from two Arabidopsis genotypes. Figure shows the different shapes of the GCs reconstructed from (a) the J0121 ≫ GFP control line, and (b) the J0121 ≫ DTA line. Note that all GCs from both lines show the typically irregular shape described for the wild-type cells in Supporting Information Fig. S1.

Arabidopsis lines, with high confidence that the results obtained are representative of the differences in the total volume occupied by the GCs.

In conclusion, there is an increasing need for standardized methods to accurately phenotype GCs, particularly when evaluating gene function in mutant or transgenic plants. Here, we obtained for the first time 3D models and volumes of 162 GCs from galls induced in Arabidopsis by *M. javanica*. These data provided the basis on which to develop a simple method based on 2D images of thin and thick gall sections that showed a high correlation to the volume of the reconstructed GCs. The utility of the simplified method was confirmed in a particular transgenic line compared with a control line (J0121 ≫ DTA versus J0121 ≫ GFP). Therefore, we showed that the method proposed permits data to be extracted with high confidence with respect to the volume of cells, considering the complexity and highly irregular shape of GCs. Putative methods for reconstruction and volume measurements using confocal microscopy, two-photon microscopy or SPIM would have to be adapted to the gall thickness and optical characteristics of the different tissues in the galls of each plant species, which represents a serious limitation. By contrast, the simple method that we developed, using Arabidopsis as a model, could easily be extended to different plant species and growing conditions as it is independent of gall thickness or transparency.

Acknowledgements

This work was supported by grants from the Spanish Government to C.E. (AGL2010-17388) and C.F. (CSD2007-057 and PCIN-2013-053) and the Castilla-La Mancha Government to C.F. and C.E. (PCI08-0074-0294). We are very grateful to Dr Albert Cardona for his valuable help and training with the TrakEM2 program and to María Luisa García for her technical assistance with the sectioning.

References

Abad P, Favery B, Rosso MN, Castagnone-Sereno P. 2003. Root-knot nematode parasitism and host response: molecular basis of a sophisticated interaction. *Molecular Plant Pathology* **4**: 217–224.

de Almeida Engler J, Kyndt T, Vieira P, Van Cappelle E, Boudolf V, Sanchez V, Escobar C, De Veylder L, Engler G, Abad P *et al.* 2012. *CCS52* and *DEL1* genes are key components of the endocycle in nematode-induced feeding sites. *Plant Journal* **72**: 185–198.

de Almeida Engler J, Van Poucke K, Karimi M, De Groodt R, Gheysen G, Engler G, Gheysen G. 2004. Dynamic cytoskeleton rearrangements in giant cells and syncytia of nematode-infected roots. *Plant Journal* **38**: 12–26.

Antonino de Souza JD Jr, Ramos Coelho R, Tristan Lourenco I, da Rocha Fragoso R, Barbosa Viana AA, Pepino Lima, de Macedo L, Mattar da Silva MC, Gomes Carneiro RM, Engler G *et al.* 2013. Knocking-down *Meloidogyne incognita* proteases by plant-delivered dsRNA has negative pleiotropic effect on nematode vigor. *PLoS ONE* **8**: e85364.

Anwar SA, McKenry MV. 2007. Variability in reproduction of four populations of *Meloidogyne incognita* on six cultivars of cotton. *Journal of Nematology* **39**: 105–110.

Atkinson HJ, Lilley CJ, Urwin PE. 2012. Strategies for transgenic nematode control in developed and developing world crops. *Current Opinion in Biotechnology* **23**: 251–256.

Banora MY, Rodiuc N, Baldacci-Cresp F, Smertenko A, Bleve-Zacheo T, Mellilo MT, Karimi M, Hilson P, Evrard JL, Favery B *et al.* 2011. Feeding cells induced by phytoparasitic nematodes require gamma-tubulin ring complex for microtubule reorganization. *PLoS Pathogens* **7**: e1002343.

Barcala M, Garcia A, Cabrera J, Casson S, Lindsey K, Favery B, Garcia-Casado G, Solano R, Fenoll C, Escobar C. 2010. Early transcriptomic events in microdissected Arabidopsis nematode-induced giant cells. *Plant Journal* **61**: 698–712.

Barcala M, Garcia A, Cubas P, Almoguera C, Jordano J, Fenoll C, Escobar C. 2008. Distinct heat-shock element arrangements that mediate the heat shock, but not the late-embryogenesis induction of small heat-shock proteins, correlate with promoter activation in root-knot nematode feeding cells. *Plant Molecular Biology* **66**: 151–164.

Bird AF. 1961. The ultrastructure and histochemistry of a nematode-induced giant cell. *Journal of Biophysical and Biochemical Cytology* **11**: 701–715.

Bleve-Zacheo T, Melillo LT. 1997. The biology of giant cells. In: Fenoll C, Grundler FMW, Ohl SA, eds. *Cellular and molecular aspects of plant–nematode interactions*. Dordrecht, the Netherlands: Kluwer Academic, 65–79.

Cabrera J, Barcala M, Fenoll C, Escobar C. 2014a. Transcriptomic signatures of transfer cells in early developing nematode feeding cells of Arabidopsis focused on auxin and ethylene signaling. *Frontiers in Plant Science* **5**: 107.

Cabrera J, Diaz-Manzano FE, Sanchez M, Rosso MN, Melillo T, Goh T, Fukaki H, Cabello S, Hofmann J, Fenoll C *et al.* 2014b. A role for LATERAL ORGAN BOUNDARIES-DOMAIN 16 during the interaction Arabidopsis-Meloidogyne spp. provides a molecular link between lateral root and root-knot nematode feeding site development. *New Phytologist* **203**: 632–645.

Caillaud M-C, Lecomte P, Jammes F, Quentin M, Pagnotta S, Andrio E, de Almeida Engler J, Marfaing N, Gounon P, Abad P *et al.* 2008. MAP65-3 microtubule-associated protein is essential for nematode-induced giant cell ontogenesis in *Arabidopsis*. *Plant Cell* **20**: 423–437.

Cardona A, Saalfeld S, Schindelin J, Arganda-Carreras I, Preibisch S, Longair M, Tomancak P, Hartenstein V, Douglas RJ. 2012. TrakEM2 software for neural circuit reconstruction. *PLoS ONE* **7**: e38011.

Chakraborty A, Perales MM, Reddy GV, Roy-Chowdhury AK. 2013. Adaptive geometric tessellation for 3D reconstruction of anisotropically developing cells in multilayer tissues from sparse volumetric microscopy images. *PLoS ONE* **8**: e67202.

Clement M, Ketelaar T, Rodiuc N, Banora MY, Smertenko A, Engler G, Abad P, Hussey PJ, de Almeida Engler J. 2009. Actin-depolymerizing factor2-mediated actin dynamics are essential for root-knot nematode infection of *Arabidopsis*. *Plant Cell* **21**: 2963–2979.

Das S, DeMason DA, Ehlers JD, Close TJ, Roberts PA. 2008. Histological characterization of root-knot nematode resistance in cowpea and its relation to reactive oxygen species modulation. *Journal of Experimental Botany* **59**: 1305–1313.

Escobar C, Barcala M, Portillo M, Almoguera C, Jordano J, Fenoll C. 2003. Induction of the Hahsp17.7G4 promoter by root-knot nematodes: involvement of heat-shock elements in promoter activity in giant cells. *Molecular Plant–Microbe Interactions* **16**: 1062–1068.

Fuller VL, Lilley CJ, Urwin PE. 2008. Nematode resistance. *New Phytologist* **180**: 27–44.

Gal TZ, Aussenberg ER, Burdman S, Kapulnik Y, Koltai H. 2006. Expression of a plant expansin is involved in the establishment of root knot nematode parasitism in tomato. *Planta* **224**: 155–162.

Gamborg OL, Miller RA, Ojima K. 1968. Nutrient requirements of suspension cultures of soybean root cells. *Experimental Cell Research* **50**: 151–158.

Girshovitz P, Shaked NT. 2012. Generalized cell morphological parameters based on interferometric phase microscopy and their application to cell life cycle characterization. *Biomedical Optics Express* **3**: 1757–1773.

Grandjean O, Vernoux T, Laufs P, Belcram K, Mizukami Y, Traas J. 2004. *In vivo* analysis of cell division, cell growth, and differentiation at the shoot apical meristem in Arabidopsis. *Plant Cell* **16**: 74–87.

Grundler FMW, Böckenhoff A. 1997. Physiology of nematode feeding and feeding sites. In: Fenoll C, Grundler FMW, Ohl SA, eds. *Cellular and molecular aspects of plant–nematode interactions*. Dordrecht, the Netherlands: Kluwer Academic Publishers, 107–119.

Iberkleid I, Vieira P, de Almeida Engler J, Firester K, Spiegel Y, Horowitz SB. 2013. Fatty acid-and retinol-binding protein, Mj-FAR-1 induces tomato host susceptibility to root-knot nematodes. *PLoS ONE* **8**: e64586.

Jones MGK, Dropkin VH. 1976. Scanning electron microscopy in nematode-induced giant transfer cells. *Cytobios* **15**: 149–161.

Jones MGK, Goto DB. 2011. Root-knot nematodes and giant cells. In: Jones J, Gheysen G, Fenoll C, eds. *Genomics and molecular genetics of plant–nematode interactions*. Dordrecht, the Netherlands: Springer, 83–102.

Jones MGK, Gunning BES. 1976. Transfer cells and nematode induced giant cells in *Helianthemum*. *Protoplasma* **87**: 273–279.

Jones MGK, Northcote DH. 1972. Multinucleate transfer cells induced in coleus roots by the root-knot nematode, Meloidogyne arenaria. *Protoplasma* **75**: 381–395.

Kayes JM, Clark SE. 1998. CLAVATA2, a regulator of meristem and organ development in Arabidopsis. *Development* **125**: 3843–3851.

Kyndt T, Vieira P, Gheysen G, de Almeida-Engler J. 2013. Nematode feeding sites: unique organs in plant roots. *Planta* **238**: 807–818.

Lilley CJ, Wang D, Atkinson HJ, Urwin PE. 2011. Effective delivery of a nematode-repellent peptide using a root-cap-specific promoter. *Plant Biotechnology Journal* **9**: 151–161.

Orion D, Wergin WP. 1982. Chloroplast differentiation in tomato root galls induced by the root knot nematode *Meloidogyne incognita*. *Journal of Nematology* **14**: 77–83.

Pegard A, Brizzard G, Fazari A, Soucaze O, Abad P, Djian-Caporalino C. 2005. Histological characterization of resistance to different root-knot nematode species related to phenolics accumulation in *Capsicum annuum*. *Phytopathology* **95**: 158–165.

Portillo M, Cabrera J, Lindsey K, Topping J, Andres MF, Emiliozzi M, Oliveros JC, Garcia-Casado G, Solano R, Koltai H *et al.* 2013. Distinct and conserved transcriptomic changes during nematode-induced giant cell development in tomato compared with Arabidopsis: a functional role for gene repression. *New Phytologist* **197**: 1276–1290.

Portillo M, Lindsey K, Casson S, Garcia-Casado G, Solano R, Fenoll C, Escobar C. 2009. Isolation of RNA from laser-capture-microdissected giant cells at early differentiation stages suitable for differential transcriptome analysis. *Molecular Plant Pathology* **10**: 523–535.

Schindelin J, Arganda-Carreras I, Frise E, Kaynig V, Longair M, Pietzsch T, Preibisch S, Rueden C, Saalfeld S, Schmid B *et al.* 2012. Fiji: an open-source platform for biological-image analysis. *Nature Methods* **9**: 676–682.

Schmid B, Schindelin J, Cardona A, Longair M, Heisenberg M. 2010. A high-level 3D visualization API for Java and ImageJ. *BMC Bioinformatics* **11**: 274.

Schneider CA, Rasband WS, Eliceiri KW. 2012. NIH Image to ImageJ: 25 years of image analysis. *Nature Methods* **9**: 671–675.

Souza Ddos S, de Souza JD Jr, Grossi-de-Sa M, Rocha TL, Fragoso RR, Barbosa AE, de Oliveira GR, Nakasu EY, de Sousa BA, Pires NF *et al.* 2011. Ectopic expression of a *Meloidogyne incognita* dorsal gland protein in tobacco accelerates the formation of the nematode feeding site. *Plant Science* **180**: 276–282.

Vanhaeren H, Gonzalez N, Inze D. 2010. Hide and seek: uncloaking the vegetative shoot apex of *Arabidopsis thaliana*. *Plant Journal* **63**: 541–548.

Vieira P, Engler G, de Almeida Engler J. 2012. Whole-mount confocal imaging of nuclei in giant feeding cells induced by root-knot nematodes in Arabidopsis. *New Phytologist* **195**: 488–496.

Vieira P, Escudero C, Rodiuc N, Boruc J, Russinova E, Glab N, Mota M, De Veylder L, Abad P, Engler G *et al.* 2013. Ectopic expression of Kip-related proteins restrains root-knot nematode-feeding site expansion. *New Phytologist* **199**: 505–519.

Vovlas N, Rapoport HF, Jimenez Diaz RM, Castillo P. 2005. Differences in feeding sites induced by root-knot nematodes, *Meloidogyne* spp., in chickpea. *Phytopathology* **95**: 368–375.

Wasson AP, Ramsay K, Jones MG, Mathesius U. 2009. Differing requirements for flavonoids during the formation of lateral roots, nodules and root knot nematode galls in *Medicago truncatula*. *New Phytologist* **183**: 167–179.

Wichman BA, Hill ID. 1982. Algorithm AS 183: an efficient and portable pseudo-random number generator. *Applied Statistics* **31**: 188–190.

Young KD. 2006. The selective value of bacterial shape. *Microbiology and Molecular Biology Reviews* **70**: 660–703.

Supporting Information

Additional supporting information may be found in the online version of this article.

Fig. S1 The full 3D models or reconstructions of the 162 individual GCs scored in this study.

Fig. S2 Area distribution of the GC pool from representative reconstructed galls used in the study.

Video S1 Video file explaining the three basic steps carried out during 3D reconstruction of GCs.

Video S2 Video file showing the accurate identification of the GC number during the labeling process, avoiding misinterpretations.

Please note: Wiley Blackwell are not responsible for the content or functionality of any supporting information supplied by the authors. Any queries (other than missing material) should be directed to the *New Phytologist* Central Office.